

Particle sorting by a structured microfluidic ratchet device with tunable selectivity: Theory and Experiment

Lukas Bogunovic,¹ Ralf Eichhorn,² Jan Regtmeier,¹ Dario Anselmetti,¹ and Peter Reimann^{1,*}

¹*Universität Bielefeld, Fakultät für Physik, 33615 Bielefeld, Germany*

²*NORDITA, Roslagstullsbacken 23, 106 91 Stockholm, Sweden*

(Dated: April 18, 2022)

We theoretically predict and experimentally demonstrate that several different particle species can be separated from each other by means of a ratchet device, consisting of periodically arranged triangular (ratchet) shaped obstacles. We propose an explicit algorithm for suitably tailoring the externally applied, time-dependent voltage protocol so that one or several, arbitrarily selected particle species are forced to migrate oppositely to all the remaining species. As an example we present numerical simulations for a mixture of five species, labelled according to their increasing size, so that species 2 and 4 simultaneously move in one direction and species 1, 3, and 5 in the other. The selection of species to be separated from the others can be changed at any time by simply adapting the voltage protocol. This general theoretical concept to utilize one device for many different sorting tasks is experimentally confirmed for a mixture of three colloidal particle species.

PACS numbers: 05.40.-a, 02.60.Cb, 05.10.Gg

I. INTRODUCTION

Ratchet effects refer to directed transport under non-equilibrium conditions in periodic systems with broken spatial symmetry, and are currently attracting considerable attention in a wide variety of different fields [1–4]. So far, the majority of pertinent works has been devoted to basic theoretical concepts, fueled – among others – by the exciting perspective to exploit ratchet effects for particle sorting purposes at the nano- and micro-scale. Concerning experimental ratchet devices, directed transport *per se* has been demonstrated by now in quite a number of systems as well, see refs. [5–17] for just a few examples. On the other hand, the actual sorting of different particle species has been achieved only in a few experimental systems [18–29]. All of them have been conducted in some microstructures with broken spatial symmetry, while the indispensable non-equilibrium conditions have been implemented mostly by utilizing electrokinetic effects [18–27], but also via magnetic fields [28] or intracellular morphological changes [29].

Along these lines of experimentally realizing ratchet effects by exploiting electrokinetics [30, 31], our present work addresses the natural next question: Given a mixture of different particle species, is it possible to separate any arbitrarily selected subset of species from all the others with the help of one and the same microstructured ratchet device? After setting the general framework we have in mind, we will outline the basic theoretical ideas, verify them quantitatively by numerical simulations, and finally provide the experimental proof-of-principle for a colloidal suspension containing three different species of polystyrene beads.

The general experimental framework is schematically

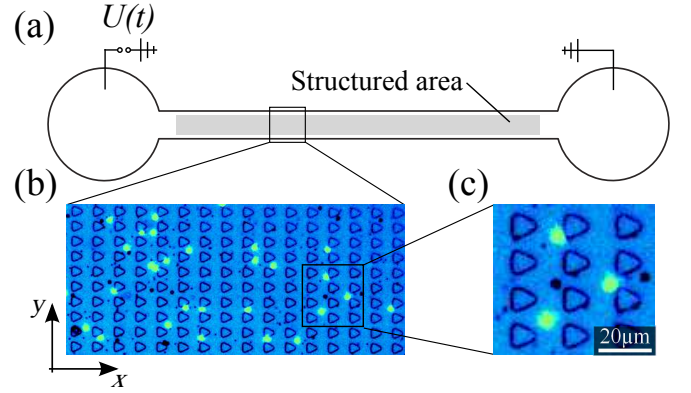


FIG. 1: Experimental setup. (a): Schematic top view (x - y -plane) of the entire device (not to scale) with reservoirs and electrodes at its ends and a central, microstructured part (grey). (b) Optical micrograph image of the microstructured area. The entire microstructured region extends over $10000\text{ }\mu\text{m} \times 300\text{ }\mu\text{m}$ in the x - y -plane and $10\text{ }\mu\text{m}$ in height (z -direction). (c) Magnification, exhibiting periodically arranged obstacles (posts) of ratchet-shaped cross section (see Fig. 2 for the dimensions of the obstacles) with a period of $20\text{ }\mu\text{m}$ in x direction and $14\text{ }\mu\text{m}$ in y direction. Also visible are microbeads of three different diameters ($2.9\text{ }\mu\text{m}$, $1.9\text{ }\mu\text{m}$, and $1.1\text{ }\mu\text{m}$). The largest and smallest beads can be easily distinguished by their size. The medium sized beads are fluorescently labelled and thus appear as bright spots.

illustrated in Fig. 1 (see also Appendix A.1). The central, topographically structured area consists of periodically arranged, triangular (ratchet) shaped obstacles. The entire device is filled with a buffer solution, containing particles in sufficiently high dilution, so that their mutual interaction is negligible. It is actuated by an external voltage like indicated in Fig. 1a.

*Electronic address: reimann@Physik.Uni-Bielefeld.DE

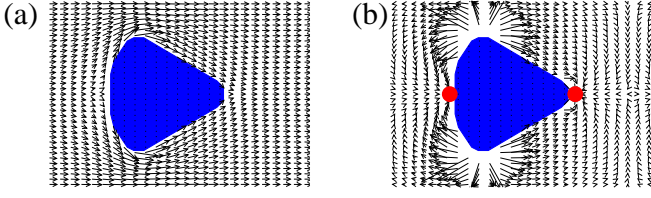


FIG. 2: Force fields. (a) Electrical field $\vec{E}_1(\vec{r})$ around one idealized obstacle within a region of size $20 \mu\text{m} \times 14 \mu\text{m}$, corresponding to one basic “unit cell” of the periodic microstructure, see also Fig. 1c and Eq. (2). The shape of the obstacle is chosen to closely approximate the real experimental shape of the triangular posts as formed by the soft lithography process (see Appendix A.1) and as characterized by REM imaging. The obstacle extends $8.5 \mu\text{m}$ from baseline to tip (x direction) and $8.5 \mu\text{m}$ from side vertex to side vertex (y direction). (b) Dielectrophoretic force field $\alpha \vec{\nabla} \vec{E}_1^2(\vec{r})/2$, under the assumption that $\alpha < 0$, see also Eq. (5) and Appendix A.5. Red dots indicate particle traps (minima of the potential (5)). Both fields inherit the spatial periodicity of the microstructure (Fig. 1b) and are depicted here in arbitrary units.

II. THEORETICAL CONCEPTS

A. Electrokinetic effects

Upon applying an electrical DC- and AC-voltage $U(t)$ of the general form

$$U(t) = U_{\text{DC}} + U_{\text{AC}} \sin(\omega t) \quad (1)$$

to the electrodes in Fig. 1a, an electrical field $\vec{E}(\vec{r}, t)$ is created at position $\vec{r} = (x, y, z)$ and time t within the device. For all experimentally realistic DC- and AC-voltages in (1), the electrostatic approximation is valid [32], so that the field induced by $U(t)$ is

$$\vec{E}(\vec{r}, t) = U(t) \vec{E}_1(\vec{r})/U_1, \quad (2)$$

where $\vec{E}_1(\vec{r})$ denotes the electrical field induced by a unit DC-voltage $U_1 := 1 \text{ V}$. To determine $\vec{E}_1(\vec{r})$ within the structured region (Fig. 1b), we numerically solved Laplace’s equation with Neumann boundary conditions, thus approximately treating the microstructure as a perfect isolator [32, 33]. The resulting electrical field $\vec{E}_1(\vec{r})$ around an experimentally realistic obstacle is illustrated in Fig. 2a. Outside the structured region, an approximate treatment along the lines of [34] was adopted to estimate the voltage drop over the structured region, given the voltage $U_1 := 1 \text{ V}$ is applied to the device electrodes (cf. Fig. 1).

Due to the electric field $\vec{E}(\vec{r}, t)$, a particle in the microstructure experiences two different electrokinetic effects [31, 35]: First, it is driven by electrophoresis. The particle velocity $\dot{\vec{r}}$ due to purely electrophoretic forces (i.e. neglecting other electrokinetic effects, thermal noise etc.) can be expressed in terms of the fluid’s permittivity

ϵ , its viscosity η , and the particle’s zeta potential ζ by the well-known Helmholtz-Smoluchowski relation

$$\dot{\vec{r}} = \vec{E}(\vec{r}, t) \epsilon \zeta / \eta, \quad (3)$$

provided the Debye screening length of the counter-ions is much smaller than the particle diameter [35, 36]. The latter condition can be safely taken for granted in view of a Debye length of $\approx 10 \text{ nm}$ for our experimental 10 mM phosphate buffer [35]. The Helmholtz-Smoluchowski relation (3) applies to particles of any shape [36] and holds also if the external electric field varies over distances comparable to the particle size [37]. We further note that it can formally be rewritten as a force balance $\gamma \dot{\vec{r}} = q^* \vec{E}(\vec{r})$ between the viscous (Stokes) friction force $\gamma \dot{\vec{r}}$ with friction coefficient γ and an effective electrostatic force $q^* \vec{E}(\vec{r})$ with an “effective charge” q^* defined as

$$q^* := \gamma \epsilon \zeta / \eta \quad (4)$$

This quantity q^* is a purely formal abbreviation which has the dimension of a charge but has very little to do with any kind of actual physical charge.

Second, the electrical field $\vec{E}(\vec{r}, t)$ induces a dipole moment \vec{p} in the particle and the ion cloud around it, which is characterized by the relevant (effective) polarizability α . In general, α is a complex, frequency dependent quantity, and the dipole moment \vec{p} may be composed of several contributions according to the frequency components contained in the electrical field $\vec{E}(\vec{r}, t)$. Under our present experimental conditions, however, the quasi-static approximation with α referring to the zero frequency limit can be invoked, since polarization processes are much faster than time-variations of the electric field [38]. Likewise, conductive and dielectric losses can be safely neglected, so that α is given as a real-valued quantity. The dipole moment \vec{p} is thus of the form $\alpha \vec{E}(\vec{r}, t)$, and the standard dipole-field-coupling force $(\vec{p} \cdot \vec{\nabla}) \vec{E}$ derives from a dielectrophoretic potential

$$W(\vec{r}, t) = -\alpha \vec{E}^2(\vec{r}, t)/2. \quad (5)$$

Figure 2b depicts the corresponding dielectrophoretic force field around an experimentally realistic obstacle. Similar as q^* , also the polarizability α is an effective quantity depending on particle and solution properties. A common approximation for the present situation of a colloidal bead (diameter d) suspended in an ionic buffer solution is

$$\alpha = -2\pi\epsilon(d/2)^3, \quad (6)$$

obtained from the well-known basic formula for the polarization of a non-conducting dielectric sphere in a conducting dielectric medium with permittivity ϵ at low frequencies of the electric field [38].

B. Particle dynamics

In addition to the two electrokinetic effects from the previous Section, other relevant forces acting on the par-

ticle are thermal fluctuations and interactions with the microstructure, while inertia effects are so tiny that they do not play any noticeable role [35, 39]. We model the particle dynamics by the standard overdamped Langevin equation [1–4, 18–24, 26, 27, 32, 33]

$$\gamma \dot{\vec{r}} = q^* \vec{E}(\vec{r}, t) + \alpha \vec{\nabla} \vec{E}^2(\vec{r}, t)/2 + \vec{F}(\vec{r}) + \vec{\xi}(t). \quad (7)$$

On the right hand side, the first and second terms are the electrophoretic and dielectrophoretic forces as detailed above. The third term $\vec{F}(\vec{r})$ accounts for the repulsion by the microstructure, idealized as hard wall forces due to the periodic obstacles from Fig. 2 and the channel walls. The last term $\vec{\xi}(t)$ describes thermal fluctuations. Its components $\xi_\sigma(t)$, $\sigma \in \{x, y, z\}$, are modeled as usual [1–4] by independent Gaussian noises of zero average and correlation $\langle \xi_\sigma(t) \xi_\sigma(s) \rangle = 2\gamma kT \delta(t-s)$, where k is Boltzmann’s constant, $T \approx 290$ K the ambient temperature, and where $\langle \cdot \rangle$ denotes the average over many realizations of the Gaussian noise. The quantitative values of the remaining model parameters γ , q^* , and α are provided in the Appendices A.2–A.4.

The model (7) follows the standard approach for describing electrokinetic effects and thus neglects non-linear terms of cubic and higher order in the external electrical field $\vec{E}(\vec{r}, t)$, which would, in particular, take into account local changes of $\vec{E}(\vec{r}, t)$ due to the presence of the particle. Likewise, hydrodynamic interactions are neglected. This approximation is justified in the present case of electrophoretically driven particle motion, because in electrophoresis hydrodynamic interactions are essentially screened [40]. Remaining hydrodynamic effects, in particular from interactions of the particle with the channel structure, are approximately taken into account by determining the friction coefficient γ from the particle diffusion in the microstructure, see Appendix A.2. Since the friction forces are dominated by hydrodynamic interactions with the bottom and top walls of the microfluidic channel (which are isotropic in x and y direction), a possible orientation dependence of the friction force in the x - y plane for particle movements parallel or perpendicular to the obstacle walls is expected to be negligibly small, and is thus omitted in our model. Ultimately, all these approximation are justified by the good agreement between the theoretical predictions and the experimental results (see, e.g., Figs. 5a and 6).

C. Separation principle

As already mentioned we want to address the problem of separating an arbitrarily selected subset of particle species from a mixture of many different particle species. Obviously, the “optimal” realization of such a separation is to move the selected subset into one direction along the microstructured channel, while, at the same time, all the remaining species migrate into the opposite direction. In

other words, the average particle velocity in x direction

$$v := \lim_{t \rightarrow \infty} \frac{\langle x(t) - x(0) \rangle}{t} \quad (8)$$

assumes different signs for the two sets of particle species. In the following, we devise the theoretical idea how this task can be accomplished with our microfluidic device from Fig. 1 by applying a periodic sequence of combined DC- and AC-voltage pulses.

To keep things as simple as possible, we focus on cases where the DC-voltage mainly determines the electrophoresis, while the AC-voltage predominantly rules the dielectrophoresis. More precisely, we restrict ourselves to DC- and AC-voltages in (1) such that practically only the “systematic” DC-voltage U_{DC} contributes to the electrophoretic force $q^* \vec{E}(\vec{r}, t)$, while the effects of the “oscillating” AC-driving $U_{\text{AC}} \sin(\omega t)$ occur on time- and length-scales, which are of no relevance for the effects we are interested in, and practically average out to zero during one oscillation. On the other hand, combining Eqs. (1), (2) and (5) we see that the time-averaged dielectrophoretic force $\alpha \vec{\nabla} \vec{E}^2(\vec{r}, t)/2$ is proportional to $\alpha \vec{\nabla} \vec{E}_1^2(\vec{r})(U_{\text{DC}}^2 + U_{\text{AC}}^2)/U_1^2 = \alpha \vec{\nabla} \vec{E}_1^2(\vec{r})(1 + U_{\text{DC}}^2/U_{\text{AC}}^2)(U_{\text{AC}}^2/U_1^2)$. For $|U_{\text{DC}}| \ll |U_{\text{AC}}|$ and sufficiently large U_{AC} , the DC-contribution to the dielectrophoretic force $\alpha \vec{\nabla} \vec{E}^2(\vec{r}, t)/2$ can always be safely neglected, while the net effect of the AC-contribution over one oscillation will still be significant. In other words, electrophoresis is governed by the DC- and dielectrophoresis by the AC-voltage. In practice, these conditions are met by restricting ourselves to relatively small DC-voltages (a few volts in the experiment), while U_{AC} may be substantially larger (several hundred volts). The AC frequencies $\omega/2\pi$ are restricted to the range of several hundreds up to thousands of Hz (a frequency of $\omega/2\pi = 100$ Hz turned out to be optimal for performing the experiments), thus also guaranteeing that the quasi-static approximation for α is valid (see also Sec. 2.1).

From Fig. 2 we can infer that the electrophoretic forces alone would generate a net particle motion along the x -axis. On the other hand, the dielectrophoretic forces give rise to “particle traps” (attractors, deriving from local minima of the dielectrophoretic potential (5)). Neglecting thermal noise effects for a moment, we are thus faced with a competition between directed motion (governed by the DC-voltage) and trapping (governed by the AC-voltage). Depending on the relative magnitudes of U_{DC} and U_{AC} , either the directed particle motion “wins” or the particle stays trapped. As a result, the entire parameter space spanned by the DC- and the AC-voltage – henceforth denoted as “DC-AC-voltage plane” – can be divided into regions with steady particle motion and regions where the particle stands still, see Fig. 3a. Observing that the electrophoretic forces are proportional to $q^* U_{\text{DC}}$ and the dielectrophoretic forces proportional to αU_{AC}^2 , the borderlines between those regions are gov-

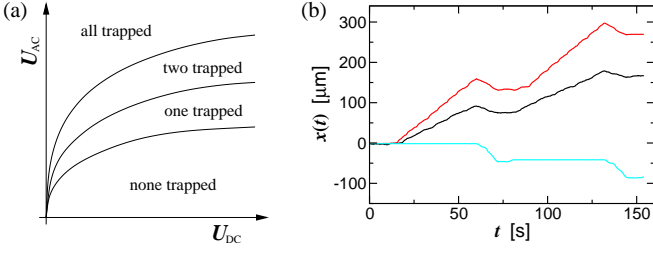


FIG. 3: Theoretical concept. (a) Qualitative sketch of the parameter space spanned by the DC- and AC-voltage with n moving and $N - n$ trapped particle species for $N = 3$ (see main text). The particle is trapped as long as the combined deterministic electrokinetic effects result in potential minima close to the obstacles (see Fig. 2b and main text), i.e. at the border between two different trapping regions (indicated by the solid lines), the potential minima just disappear for one of the particle species. Thermal noise effects are neglected in that picture; they would result in a *finite* trapping time which for that particle species approaches zero close to border, but grows exponentially with the depth of the potential minima when moving away from the border into the trapping region towards larger U_{AC} or smaller U_{DC} . For negative U_{AC} , the regions are symmetric (see (9)) and hence omitted in the present plot. For negative U_{DC} , Eq. (9) implies an analogous symmetry apart from a different proportionality constant c . (b) Numerical solutions of (7) for particles with diameters $1.1 \mu\text{m}$ (black), $1.9 \mu\text{m}$ (red), and $2.9 \mu\text{m}$ (blue), moving in a periodically continued array of ratchet shaped obstacles as depicted in Fig. 2. The external driving is specified by Eqs. (1), (2) and by Table 1, protocol a. Remaining parameter values and simulation details: see Appendices A.2-A.4 and A.5.

erned by the equation

$$U_{AC}^2 = c |q^* U_{DC} / \alpha| \quad (9)$$

with a proportionality constant c which depends on the details of the microstructure (“forming” the spatial variations of the electric field), the particle size, the sign of α , and – in case of asymmetric (ratchet shaped) obstacles – on the direction of the electrophoretic forces and thus on the sign of $q^* U_{DC}$, but otherwise is independent of q^* , α , U_{DC} , and U_{AC} .

The main consequence is that for two particles species with different ratios q^*/α or different sizes, the borderlines (9) between motion and trapping are different. (Here and in all what follows, we tacitly focus on the case that q^* and α have the same sign for all species). As a consequence, the DC-AC-voltage plane now divides into regions with (i) both particle species moving, (ii) one moving and the other trapped, and (iii) both trapped. Likewise, for $N > 2$ particle species, the DC-AC-voltage plane exhibits regions with n moving and $N - n$ trapped species for any $n = 0, 1, 2, \dots, N$. For an example with $N = 3$, see Fig. 3a.

By exploiting the existence of these regions, we will now construct a “voltage protocol” during which any particle of species k is on average displaced by Δx_k in

x -direction, where $k = 1, \dots, N$ labels the species and the Δx_k are arbitrary (positive or negative) multiples of the lattice constant in x -direction. By repeating the corresponding protocol periodically in time, the average particle velocity (8) of species k assumes the value $\Delta x_k / \tau$, where τ denotes the duration of one period of the voltage protocol. By suitably choosing sign and modulus of the Δx_k , it is thus possible to make an arbitrarily selected subset of species move oppositely to all the others. In other words, any preset separation task can be accomplished by properly tailoring the externally applied DC- and AC-voltage.

Given the Δx_k for $k = 1, \dots, N$, the announced protocol is composed of $N + 1$ time intervals of lengths Δt_n , where $n = 0, 1, 2, \dots, N$ and $\tau = \sum_{n=0}^N \Delta t_n$. Throughout the n -th time interval, the DC- and AC-voltages are kept at constant values $U_{DC}^{(n)}$ and $U_{AC}^{(n)}$, respectively. As seen above, the actual values of $U_{DC}^{(n)}$ and $U_{AC}^{(n)}$ can and will be chosen so that n particle species are moving and $N - n$ are trapped. Furthermore, the indices $k = 1, \dots, N$ of the particle species can be chosen without loss of generality so that those with $k \leq n$ are moving during time interval n and those with $k > n$ stay trapped. Put differently, particle k (i.e. a particle of species k) is moving during the time intervals with $n \geq k$ and is trapped when $n < k$. Within the respective regions of the DC-AC-voltage plane (see above), $U_{DC}^{(n)}$ and $U_{AC}^{(n)}$ can still be freely chosen. In particular, $U_{DC}^{(n)}$ may still be of either sign, and likewise the transport direction of the moving species.

We first focus on particle N , which is only moving during the last time interval. Hence, Δt_N , $U_{DC}^{(N)}$, and $U_{AC}^{(N)}$, can (and must) be chosen so that particle N covers a distance Δx_N during this time interval N . During the same time interval, all the remaining particles with $k = 1, \dots, N - 1$ are also moving. Their respective displacements may be positive or negative and are denoted by δx_k . Once we made our choice of Δt_N , $U_{DC}^{(N)}$, and $U_{AC}^{(N)}$ also the traveling distances δx_k are uniquely fixed and can be calculated quantitatively.

During all the remaining time intervals with $n = 0, \dots, N - 1$, particle N stays trapped and thus its total displacement amounts to Δx_N , as desired. On the other hand, the particles with $k = 1, \dots, N - 1$ now have to exhibit displacements by $\Delta x'_n = \Delta x_n - \delta x_n$ during the remaining time intervals with $n = 0, \dots, N - 1$. Along exactly the same line of reasoning, the existence of appropriate values of Δt_n , $U_{DC}^{(n)}$, and $U_{AC}^{(n)}$ now follows by way of induction for $n = N - 1, N - 2, \dots, 1$.

The left-over time interval with $n = 0$ may appear superfluous since all particles are trapped. It is, however, essential for the separation procedure to work efficiently. In practice, there are various complications and perturbations of the above idealized scheme, most notably thermal noise and transient effects: after each “jump” of U_{DC} and U_{AC} , every particle needs a certain “relaxation” time to

adapt its motion to the new circumstances (approach the new attractor of the dynamics), especially when switching from “trapped” to “moving” or vice versa. All these effects would prevent a reliable time-periodic particle motion upon periodically repeating the protocol without the “all-trapping” time interval $n = 0$. Moreover, it guarantees that the particles are indeed trapped before species by species is released from the traps during the next cycle of the protocol.

We emphasize that the only indispensable prerequisite of the above procedure is the existence of the different regions in the DC-AC-voltage plane (Fig. 3a), which in turn represents the generic case. Different electrophoretic mobilities of the particle species or any other special system or particle properties are not required. Accordingly, the parameters Δt_n , $U_{\text{DC}}^{(n)}$, and $U_{\text{AC}}^{(n)}$ are not yet uniquely fixed and thus can still be optimized with respect to the experimental constraints and uncertainties. Along these lines one typically ends up with alternating signs of $U_{\text{DC}}^{(n)}$ and decreasing values of $|U_{\text{AC}}^{(n)}|$ (the sign is irrelevant). Moreover, in some cases one finds that less than $N + 1$ time-intervals may already do the job, see Fig. 3b and Sec. 3.

In principle, by the above strategy one may separate particle species of arbitrary sizes or q^*/α ratios in a rather broad dynamical range. In particular, increasing noise effects for smaller particles can be kept under control by applying larger voltages and hence also enhancing the deterministic effects. Likewise, reasonably small particle-to-particle variations within one species essentially lead to a shrinking of the pertinent regions in the DC-AC-voltage plane (cf. Fig. 3a) and hence are still admissible. However, too large variations lead to a disappearance of the regions and thus to a breakdown of our approach. Analogous considerations apply to deviations from a strictly periodic microstructure. On the other hand, a mixture of particles with continuously distributed sizes or q^*/α ratios may still be sorted into certain subclasses, but a truly continuous separation is not possible.

Our general scheme would in principle also work for symmetric obstacles. Ratchet shaped obstacles have the advantage of different c -values for positive and negative DC-voltages in (9), admitting much more efficient and robust separation in practice [27]. Likewise, the above mentioned transients after each “jump” of U_{DC} and U_{AC} can be exploited to further improve the efficiency of the procedure, especially when taking into account thermal noise effects. We finally note that somewhat similar concepts in the context of ratchet effects and particle sorting have been utilized previously in Refs. [41–43].

III. RESULTS

To quantitatively verify these heuristic ideas, we perform detailed numerical simulations of the model (7), see

Appendix A.5. As a first example, we consider $N = 3$ particle species. Fig. 3a illustrates the corresponding regions in the DC-AC-voltage plane with $n = 0, 1, 2, 3$ moving and $N - n$ trapped species. Fig. 3b exemplifies the separation of one species from all the others: During an initial time-interval of 10 s (see Table 1, protocol a), all particles are trapped. During the second interval of 50 s, two species are moving forward and one remains trapped. During the last interval of 12 s, all move, but now into the negative direction. Upon periodically repeating the protocol (two periods are shown), two species acquire a positive and one a negative average velocity. (An interval with only one moving species is not needed for this specific separation task.) By suitably tailored protocols (see Table 1), also any other of the three particle species can be made to migrate oppositely to the others, as will be experimentally demonstrated below.

Before doing so, a second illustration with $N = 5$ particle species is presented with Fig. 4. Proceeding as detailed above, we have tailored voltage protocols for three separation tasks which appeared to us particularly interesting and non-trivial: Fig. 4a demonstrates the separation of the middle sized particles from the two bigger and the two smaller species. Fig. 4b shows how the largest and smallest particle species can be made to move oppositely to the three middle sized species. The most challenging case is shown in Fig. 4c, namely the disentanglement of the particles with $1\text{ }\mu\text{m}$, $2\text{ }\mu\text{m}$, and $3\text{ }\mu\text{m}$ diameter from those with $1.5\text{ }\mu\text{m}$ and $2.5\text{ }\mu\text{m}$ diameter.

Closer inspection of Figs. 4a-c reveals that the particle motion does not always precisely follow the displacement pattern anticipated in the construction of the voltage protocol as described above (Sec. 2.3), but rather shows significant variations between different periods of the protocol. For instance, the $2\text{ }\mu\text{m}$ (green) particle in Fig. 4c moves in four (out of the six) voltage steps during the first period and only in three during the second period. Likewise, the $2.5\text{ }\mu\text{m}$ (blue) particle shows a net displacement of about $30\text{ }\mu\text{m}$ during the first cycle but performs no net movement in the second cycle. These variations are due to thermal noise effects, which have a strong impact on the escape process out of the dielectrophoretic traps, because these are located close to stagnation points of the DC electric field (see Fig. 2). Due to this variability of the net displacement per voltage cycle, particles of the same species are spread out along their direction of systematic motion farther than by pure thermal diffusion. Such enhanced dispersion notwithstanding, efficient particle fractionation based on transport in opposite directions is demonstrated by Fig. 4d for all three separation tasks from Figs. 4a-c. Note that even within the subsets of particle species, that have been selected to migrate in one specific direction, different migration velocities for different species and thus (partial) separation may be observed (e.g. in the first panel of Fig. 4d). This “side-effect” results from performing the separation by less than $N + 1$ steps in the voltage protocol, so that the displacements Δx_k have not been determined and opti-

TABLE I: Voltage protocols for the simulations in Figs. 3b, 6 and the experiments in Fig. 5. Listed are the voltages U_{DC} and U_{AC} in volts and the time-intervals Δt_n in seconds during which they were kept at those constant values. The entire protocol $U(t)$ in (1) is obtained by periodically cycling through the listed sequence of time-intervals. In all cases, the AC-driving frequency in (1) is set to $\omega/2\pi = 100$ Hz.

Protocol a			Protocol b			Protocol c		
Δt_n	U_{DC}	U_{AC}	Δt_n	U_{DC}	U_{AC}	Δt_n	U_{DC}	U_{AC}
10	0	400	10	0	400	10	0	400
50	-15	320	90	+15	400	40	+15	360
12	+10	0	25	-16	330	12	-10	0
			10	+10	0			

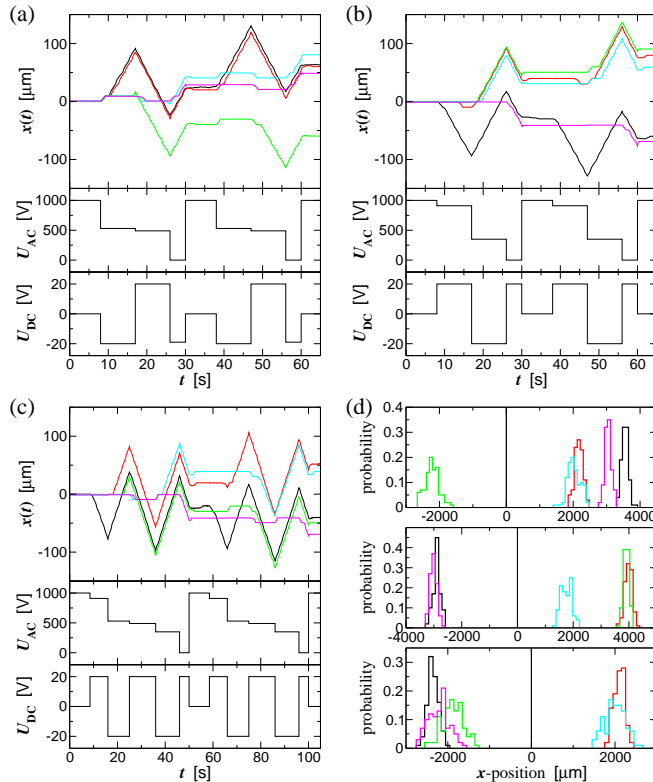


FIG. 4: Numerical solutions for 5 particles with diameters $1\mu\text{m}$ (black), $1.5\mu\text{m}$ (red), $2\mu\text{m}$ (green), $2.5\mu\text{m}$ (blue), and $3\mu\text{m}$ (magenta). (a): Separation of the $2\mu\text{m}$ particles (middle size) from all the other. (b): Separation of the smallest and largest ($1\mu\text{m}$ and $3\mu\text{m}$) particles from all the others (3 intermediate diameters). (c): Separation of the particles with $1\mu\text{m}$, $2\mu\text{m}$, and $3\mu\text{m}$ diameter from those with $1.5\mu\text{m}$ and $2.5\mu\text{m}$ diameter. The lower panels specify the voltage protocols used to achieve the separation tasks shown in the respective upper panels. In each case, two periods of the voltage protocols are shown. The explicit algorithm to devise those protocols is given in the main text. Further details and parameter values are as in Fig. 3b, see also Appendices A.2-A.5. (d): Spatial distributions of 100 particles of each species obtained after simulating 100 periods of the voltage protocols. The upper panel corresponds to the separation task from (a), the middle panel to (b), and the lower panel to (c).

mized independently for all the species in the subset (see the algorithm for constructing the voltage protocols, as described in Sec. 2.3), and from the fact that the deviations from the anticipated displacement patterns depend on particle properties and are thus different for different particle species within one subset.

Next, we turn to the experimental test of our theoretical concepts by means of the setup as detailed above in Fig. 1 and in Appendix A.1. Fig. 5 summarizes our main findings, demonstrating that for a colloidal suspension containing three different species of polystyrene beads it is indeed possible to control the transport directions to the extent that any one of the three species can be made to propagate oppositely to the other two species.

Finally, Fig. 6 shows numerical simulations, obtained along the very same lines as in Fig. 3b, except that the so generated numerical data have now been further processed exactly as the experimental data in Fig. 5a. These numerical results in Fig. 6 compare very well with the experimental counterparts from Fig. 5a. The fact that the velocity spreads in Fig. 5a are not significantly larger than in Fig. 6 implies that these experimental spreads are mainly caused by the thermal noise effects discussed above and not by variations of q^* , α , and γ for beads of the same species. The minor remaining differences between experiment and simulations are probably due to nonlinear (induced-charge) electrokinetic effects [44, 45], which we have neglected in our model (7). Furthermore, it can not be fully excluded that (small) Joule heating effects [46] affect the particle motion, although we do not observe any of the typical indicators for Joule heating during the experiments, like vortex-like flow patterns at the constrictions created by the obstacles [47, 48] or the generation of gas bubbles.

IV. CONCLUSIONS

In summary, we have put forward a new concept for particle sorting in a microstructured ratchet device by exploiting a subtle competition between electrophoretic and dielectrophoretic forces. Within one and the same device, by tailoring the applied voltage protocol, one or several arbitrarily selected particle species can be made to prop-

agate oppositely to all the other particle species. The choice of those particular species can be easily changed and adapted at any time, even while the experiment is running, by simply adapting the applied voltage protocol.

Such versatile particle transport is achieved by exploiting all “elementary ways of symmetry breaking” in the context of ratchet effects [1–4], namely spatial symmetry breaking, temporal (or dynamical) symmetry breaking, and application of a bias force. Any demand to maintain certain symmetries would amount to an unnecessary constraint, whereas their combined breaking allows for the required flexibility and efficiency [27].

Our new separation concept has been devised theoretically and realized experimentally within a particle density regime, in which particle interactions other than excluded volume effects are negligible and in which the number of dielectrophoretic particle traps is larger or comparable to the total number of particles in the microfluidic device.

In the future, experiments with biological complexes ranging from single biopolymers, like DNA or proteins, to whole cells, as well as non-biological objects, like

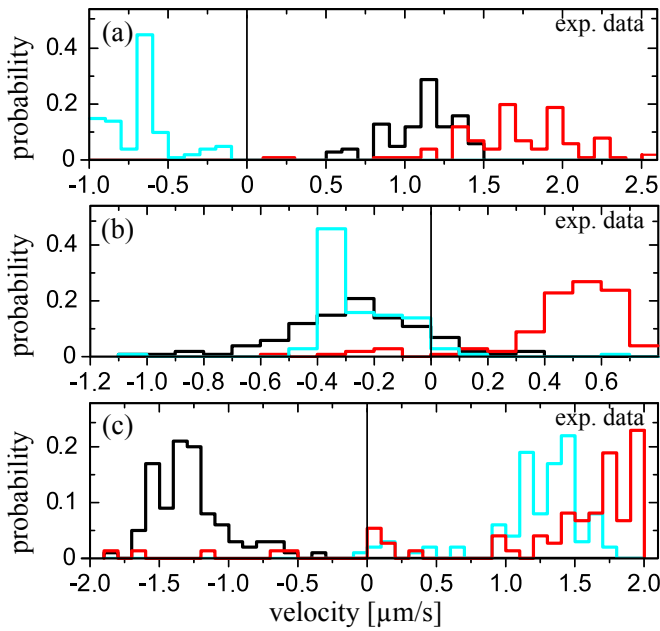


FIG. 5: Experimentally measured velocity histograms for $N = 3$ particle species (polystyrene beads with diameters $1.1\ \mu\text{m}$ (black), $1.9\ \mu\text{m}$ (red), and $2.9\ \mu\text{m}$ (blue)), simultaneously moving in the structured microfluidic ratchet device from Fig. 1. (a)-(c) show the results for the three different time-periodic voltage protocols from Table 1. For each histogram, the displacement of 100 beads in x -direction during one time-period τ of the driving voltage has been measured and interpreted as their net velocity during that driving period, i.e. an average over the histogram for a specific particle species gives the average velocity (8) for that species. In (a), the $2.9\ \mu\text{m}$ beads move oppositely to the other two species with very high reliability, and analogously for the $1.9\ \mu\text{m}$ beads in (b) and the $1.1\ \mu\text{m}$ beads in (c).

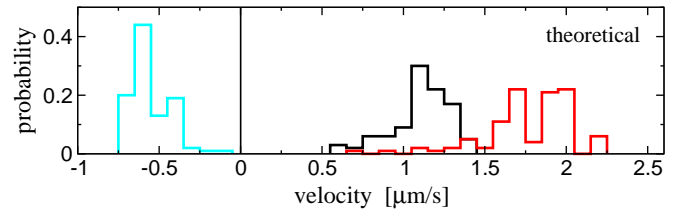


FIG. 6: Velocity histograms by numerically simulating the experiment from Fig. 5a according to (1), (7), and Table 1.

carbon-nanotubes, can be envisioned. In spite of the fact that dielectrophoretic forces are theoretically expected to strongly decrease with particle size (cf. Eq. (6)), the feasibility of manipulating single proteins by electrodeless dielectrophoresis has already been experimentally demonstrated e.g. in [49–51]. Moreover, separation may be performed not only according to size but also according to molecule conformation or particle shape [52] and thus represents a considerable advance beyond conventional separation techniques, like (pulsed-field) gel electrophoresis. A further interesting direction for future research are hydrodynamic and other interaction effects as well as possible modifications of the separation mechanism, arising for substantially higher particle densities than in our present experiments.

This work was supported by Deutsche Forschungsgemeinschaft under SFB 613 and RE1344/5-1

Appendix A: Materials and Methods

1. Experimental details

The entire microdevice (see third paragraph and Fig. 1) was cast with poly(dimethylsiloxane) (PDMS), mounted on a PDMS coated coverslip after a treatment with an oxygen plasma for 30s, and coated with a commercial triblock copolymer (F108, $500\ \mu\text{M}$) for 2 hours [53]. Spherical polystyrene beads (Molecular Probes) with diameters $1.1\ \mu\text{m}$, $1.9\ \mu\text{m}$, and $2.9\ \mu\text{m}$ at a concentration of 50 - 500 particles per species and nanoliter were immersed in a 10 mM phosphate buffer (pH 8.3) containing $200\ \mu\text{M}$ Tween 20. Hence, observable hydrodynamic or other interaction effects were always negligibly rare. For a more detailed description of our PDMS chip fabrication, particle and microstructure pre-treatment, we refer to [54, 55]. Note, that the F108 coating of the microstructure strongly suppresses electroosmotic effects [53], as well as adhesion of the polystyrene beads to the PDMS surfaces (in the experiments less than 1% of the particles got stuck to the PDMS structure). Particle tracking by video microscopy was carried out with a standard fluorescence microscope. We recorded the motion of the particles within a field of view of about $825\ \mu\text{m} \times 310\ \mu\text{m}$ with a frame-rate of 5 fps. Using the software ImageJ 1.43 (with the plugin MtrackJ) [56, 57],

particle trajectories were extracted from the recorded videos with a spatial resolution of $0.6\text{ }\mu\text{m}$ (both in x and y direction) and a temporal precision of 0.2 s . The three different particle species were easily distinguishable by their size and/or fluorescent labeling (Fig. 1c). The histogram plots in Fig. 5 were obtained from the trajectories by determining the particle displacements during one period of the voltage protocol; the so obtained velocities have a relative error below 10%.

2. Friction coefficient

For a spherical particle with diameter d in a fluid of viscosity η and infinitely far boundaries, the friction coefficient γ in Eq. (7) could be approximated by Stokes' formula $\gamma_{\text{Stokes}} = 6\pi\eta(d/2)$. Here, we go one step beyond this approximation, accounting very roughly for the hydrodynamic interactions with the microstructure by experimentally determining the diffusion coefficient D and then inferring γ from Einstein's relation $D = kT/\gamma$. Those experimentally estimated values were $D = 0.202 \pm 0.002\text{ }\mu\text{m}^2/\text{s}$ for the $1.1\text{ }\mu\text{m}$ particles, $D = 0.131 \pm 0.005\text{ }\mu\text{m}^2/\text{s}$ for the $1.9\text{ }\mu\text{m}$ particles, and $D = 0.082 \pm 0.007\text{ }\mu\text{m}^2/\text{s}$ for the $2.9\text{ }\mu\text{m}$ particles. The resulting γ -values are close to $1.7 \cdot \gamma_{\text{Stokes}}$ in all three cases. For the five particle species simulated in Fig. 4 we thus assume along the same line of reasoning that $\gamma = 1.7 \cdot \gamma_{\text{Stokes}}$.

3. Effective charge

The effective charge q^* from (4) depends in a very complicated way on the particle material, the buffer solution, and the surface coating of particle and microstructure [33, 35, 58]. In principle, one would expect that particles which only differ by their diameter have the same zeta potential, and hence the effective charge (4) would inherit the linear dependence on the particle diameter from the friction coefficient γ . In practice, even nominally identical particles but purchased at different times or from different companies are found to exhibit different electrophoretic mobilities due to somewhat differing production conditions and also due to ageing effects of the surface coating (induced by hardly controllable (bio-)chemical reactions at the particle-fluid interface). In view of these practical problems, we have directly estimated q^* by fitting the model (7) to the experimentally observed particle motion, resulting in $q^* = -0.055 \cdot 10^{-15}\text{ C}$ for the $1.1\text{ }\mu\text{m}$ particles, $q^* = -0.17 \cdot 10^{-15}\text{ C}$ for the $1.9\text{ }\mu\text{m}$ particles, and $q^* = -0.50 \cdot 10^{-15}\text{ C}$ for the $2.9\text{ }\mu\text{m}$ particles.

For the five particle species simulated in Fig. 4, we assumed – in the absence of experimental data – the above mentioned idealized theoretical situation of identical zeta potentials and thus identical Helmholtz-Smoluchowski velocities (3). In the concomitant linear dependence of

q^* on the particle diameter, the proportionality constant was chosen so as to yield a net velocity of $6\text{ }\mu\text{m/s}$ in x -direction when driven by a purely static voltage of $U_{\text{DC}} = 10\text{ V}$. This velocity is close to those we observed for the three experimental particle species.

We remark that the electroosmotic fluid flow $\vec{v}(\vec{r})$ of the ionic liquid exhibits a remarkable “similitude” to the electrophoretic Helmholtz-Smoluchowski relation (3), namely $\vec{v}(\vec{r}) = -\vec{E}(\vec{r})\epsilon\zeta'/\eta$, where ζ' is the zeta potential of the microstructure, see [58, 59] and further references therein. The effect of this electroosmotic flow on the particle can be readily incorporated into the above mentioned effective electrostatic force $q^*\vec{E}(\vec{r})$ by replacing ζ in the definition (4) by $\zeta - \zeta'$. In our actual experiment, those electroosmotic effects are, however, strongly suppressed by the F108-coating of the microstructure (see above).

4. Effective polarizability

While the particle polarizability is in general frequency dependent, experimentally we always work in the quasi-static regime ($\omega/2\pi = 100\text{ Hz}$), and hence our α always refers to the zero frequency limit. Invoking the basic formula (6) and approximating the medium's permittivity ϵ by that of water, $\epsilon = 80\epsilon_0$ (ϵ_0 being the vacuum dielectric constant), one finds that $\alpha = -7.4 \cdot 10^{-28}\text{ Fm}^2$ for the $1.1\text{ }\mu\text{m}$ particles, $\alpha = -38 \cdot 10^{-28}\text{ Fm}^2$ for the $1.9\text{ }\mu\text{m}$ particles, and $\alpha = -136 \cdot 10^{-28}\text{ Fm}^2$ for the $2.9\text{ }\mu\text{m}$ particles. The negative sign of α is in agreement with previous experiments under comparable conditions and has been tacitly anticipated in Fig. 2b.

However, the basic formula (6) neglects, among others, the polarizability of the counter-ion cloud (Debye layer) around the dielectric sphere, which, in turn, is much more difficult to estimate theoretically. Like for the above discussed effective charges, we therefore estimated the relevant effective polarizabilities by directly fitting the experimentally observed particle motion to the theoretical dynamics from Eq. (7), resulting in $\alpha = -4.0 \cdot 10^{-28}\text{ Fm}^2$ for the $1.1\text{ }\mu\text{m}$ particles, $\alpha = -27 \cdot 10^{-28}\text{ Fm}^2$ for the $1.9\text{ }\mu\text{m}$ particles, and $\alpha = -126 \cdot 10^{-28}\text{ Fm}^2$ for the $2.9\text{ }\mu\text{m}$ particles. The slight systematic deviations from (6) are remarkably small. For this reason and due to the lack of experimental data, the polarizabilities for the five particle species simulated in Fig. 4 were chosen according to formula (6) without any further corrections.

5. Simulation details

For numerical simulations, the model (7) was discretized according to the Euler algorithm with a time step of $dt = 10\text{ }\mu\text{s}$. The electric field $\vec{E}_1(\vec{r})$ and the dielectrophoretic “field” $\vec{\nabla}\vec{E}_1^2(\vec{r})$ was computed on a spatial grid with step sizes $0.02\text{ }\mu\text{m}$ within one basic “unit cell” of

the microstructure around an obstacle (cf. Figs. 2a,b) by using the COMSOL Multiphysics software suite. This was done once before performing the dynamic simulations based on (7). The actual electrophoretic and dielectrophoretic forces at the current particle position during the simulations were determined by periodically continuing the fields within this “unit cell” (in x and y direction), by interpolating linearly between the relevant grid points, and by taking into account (2). The term $\vec{F}(\vec{r})$ in (7), representing idealized hard-wall interactions with the microstructure, was treated according to the so-called rejection scheme [60]. The triangular posts of the

microstructure were approximated by the shape shown in Fig. 2.

To obtain the simulation results of Fig. 4, 100 independent realizations were computed for each particle species over 100 periods of the respective voltage protocol (the Figs. 4a-c show one typical realization for each particle species during the first two driving periods). In Fig. 6, the results of 100 independent realizations for each particle species are shown, evaluated over one period of the voltage protocol (in accordance with the processing of the experimental data).

-
- [1] F. Jülicher, A. Ajdari, J. Prost, *Rev. Mod. Phys.*, 1997, **69**, 1269–1282.
 - [2] R. D. Astumian, *Science*, 1997, **276**, 917–922.
 - [3] P. Reimann, *Phys. Rep.*, 2002, **361**, 57–265.
 - [4] P. Hänggi, F. Marchesoni *Rev. Mod. Phys.*, 2009, **81**, 387–442.
 - [5] J. Rousselet, L. Salome, A. Ajdari, J. Prost, *Nature*, 1994, **370**, 446–447.
 - [6] L. P. Faucheux, L. S. Bourdieu, P. D. Kaplan, A. Libchaber, *Phys. Rev. Lett.*, 1995, **74**, 1504–1507.
 - [7] H. Linke *et al.*, *Science*, 1999, **286**, 2314–2317.
 - [8] J. S. Bader *et al.*, *Proc. Natl. Acad. Sci. (USA)*, 1999, **96**, 13165–13169.
 - [9] J. E. Villegas *et al.*, *Science*, 2003, **302**, 1188–1191.
 - [10] S. Ghosh, A. K. Sood, N. Kumar, *Science*, 2003, **299**, 1042–1044.
 - [11] S. Matthias, F. Müller, *Nature*, 2003, **424**, 53–57.
 - [12] J. V. Hernández, E. R. Kay, D. A. Leigh, *Science*, 2004, **306**, 1532–1537.
 - [13] S. H. Lee, K. Ladavac, M. Polin, D. G. Grier, *Phys. Rev. Lett.*, 2005, **94**, 110601.
 - [14] D. Cole D *et al.*, *Nature Materials*, 2006, **5**, 305–311.
 - [15] C. C. de Souza Silva, J. van de Vondel, M. Morelle, V. V. Moshchalkov, *Nature*, 2006, **440**, 651–654.
 - [16] A. Pérez-Junquera A *et al.*, *Phys. Rev. Lett.*, 2008, **100**, 037203.
 - [17] G. Lambert, D. Liao, R. H. Austin, *Phys. Rev. Lett.*, 2010, **104**, 168102.
 - [18] L. P. Faucheux, A. Libchaber, *J. Chem. Soc. Faraday Trans.*, 1995, **91**, 3163–3166.
 - [19] L. Gorre-Talini, S. Jeanjean, P. Silberzan, *Phys. Rev. E*, 1997, **56**, 2025–2034.
 - [20] L. Gorre-Talini, J. P. Spatz, P. Silberzan, *Chaos*, 1998, **8**, 650–656.
 - [21] A. van Oudenaarden A, S. G. Boxer, *Science*, 1999, **285**, 1046–1048.
 - [22] C. Marquet, A. Buguin, L. Talini, P. Silberzan, *Phys. Rev. Lett.*, 2002, **88**, 168301.
 - [23] L. R. Huang *et al.*, *Phys. Rev. Lett.*, 2002, **89**, 178301.
 - [24] L. R. Huang, E. C. Cox, R. H. Austin, J. C. Sturm, *Science*, 2004, **304**, 987–990.
 - [25] S. Choi, J. K. Park, *Lab on a Chip*, 2005, **5**, 1161–1167.
 - [26] K. Loutharback, J. Puchalla, R. H. Austin, J. C. Sturm, *Phys. Rev. Lett.*, 2009, **102**, 045301.
 - [27] K. Loutharback *et al.*, *Microfluid. Nanofluid.*, 2010, **9**, 1143–1149.
 - [28] P. Tierno, S. V. Reddy, M. G. Roper, T. H. Johansen, T. M. Fischer, *J. Phys. Chem. B*, 2008, **112**, 3833–3837.
 - [29] G. Mahmud *et al.*, *Nature Physics*, 2009, **5**, 606–612.
 - [30] R. Pethig, G. H. Markx, *Trends in Biotechnology*, 1997, **15**, 426–432.
 - [31] P. R. C. Gascoyne, J. Vykoukal, *Electrophoresis*, 2002, **23**, 1973–1983.
 - [32] J. Regtmeier, R. Eichhorn, M. Viefhues, L. Bogunovic, D. Anselmetti, *Electrophoresis*, 2011, **32**, 2253–2273 and 3090.
 - [33] R. Eichhorn *et al.*, *Eur. Phys. J. special topics*, 2007, **143**, 159–164.
 - [34] J. Regtmeier, T. T. Duong, R. Eichhorn, D. Anselmetti, A. Ros, *Anal. Chem.*, 2007, **79**, 3925–3932.
 - [35] T. M. Squires, S. R. Quake, *Rev. Mod. Phys.*, 2005, **77**, 977–1026.
 - [36] F. A. Morrison, *J. Colloid Interface Sci.*, 1970, **34**, 210–214.
 - [37] H. J. Keh, J. L. Anderson *J. Fluid. Mech.*, 1985, **153**, 417–439.
 - [38] R. Pethig, *Biomicrofluidics*, 2010, **4**, 022811.
 - [39] E. M. Purcell, *Am. J. Phys.*, 1977, **45**, 3–11.
 - [40] D. Long, J.-L. Viovy, A. Ajdari, *Phys. Rev. Lett.*, 1996, **76**, 3858.
 - [41] A. Ajdari, D. Mukamel, L. Peliti, J. Prost, *J. Phys. I France*, 1994, **4**, 1551–1561.
 - [42] M. Schreier, P. Reimann, P. Hänggi, E. Pollak, *Europhys. Lett.*, 1998, **44**, 416–422.
 - [43] H. H. Cui, J. Voldman, X. F. Hea, K. M. Lim, *Lab on a Chip*, 2009, **9**, 2306–2312.
 - [44] V. Shilov, S. Barany, C. Grosse, O. Shramko, *Adv. Colloid. Interface Sci.*, 2003, **104**, 159–173.
 - [45] M. Z. Bazant, T. M. Squires, *Curr. Opin. Coll. Interf. Sci.*, 2010, **15**, 203–213.
 - [46] X. Xuan, *Electrophoresis*, 2008, **29**, 33–43.
 - [47] B. G. Hawkins, B. J. Kirby, *Electrophoresis*, 2010, **31**, 3622–3633.
 - [48] S. Sridharan, J. Zhu, G. Hu, X. Xuan, *Electrophoresis*, 2011, **32**, 2274–2281.
 - [49] R. W. Clarke, S. S. White, D. Zhou, L. Ying, D. Klenerman, *Angew. Chem. Int. Ed.*, 2005, **44**, 3747–3750.
 - [50] R. W. Clarke, J. D. Piper, L. Ying, D. Klenerman, *Phys. Rev. Lett.*, 2005, **98**, 198102.
 - [51] B. H. Lapizco-Encinas, S. Ozuna-Chacon, M. Rito-Palomares, *J. Chromatogr. A*, 2008, **1206**, 45–51.
 - [52] J. Regtmeier, R. Eichhorn, L. Bogunovic, A. Ros,

- D. Anselmetti, *Anal. Chem.*, 2010, **82**, 7141–7149.
- [53] W. Hellmich, J. Regtmeier, T. T. Duong, D. Anselmetti, A. Ros, *Langmuir*, 2005, **21**, 7551–7557.
- [54] T. T. Duong *et al.*, *Microelectron. Eng.*, 2003, **67-68**, 905–912.
- [55] J. Regtmeier *et al.*, *Eur. Phys. J. E*, 2007, **22**, 335–340.
- [56] M. D. Abramoff, P. J. Magalhaes, S. J. Ram, *Biophotonics Int.*, 2004, **11**, 36–42.
- [57] E. Meijering, O. Dzyubachyk, I. Smal, in: *Methods for Cell and Particle Tracking. Methods in Enzymology: Live Cell Imaging* (ed. P. M. Conn, Elsevier, in press).
- [58] E. B. Cummings, S. K. Griffiths, R. H. Nilson, P. H. Paul, *Anal. Chem.*, 2000, **72**, 2526–2532.
- [59] J. G. Santiago, *Anal. Chem.*, 2001, **73**, 2353–2365.
- [60] H. Behringer, R. Eichhorn, *Phys. Rev. E*, 2011, **83**, 065701(R).